Bound-to-continuum absorption with tunneling in type-II nanostructures: a multiband source-radiation approach

Chi-Ti Hsieh[1] and Shu-Wei Chang[1, 2, *]

[1]*Research Center for Applied Sciences, Academia Sinica, Nankang, Taipei 11529, Taiwan*
[2]*Department of Photonics, National Chiao-Tung University, Hsinchu 30010, Taiwan*

[*]swchang@sinica.edu.tw

Abstract: We convert calculations of the bound-to-continuum absorption in type-II semiconductor quantum wells into an equivalent source-radiation problem under the effective-mass approximation with band mixing. Perfectly matched layers corresponding to the eight-band Luttinger-Kohn Hamiltonian are introduced to incorporate the effect of quasi-bound states in open regions. In this way, the interplay between quantum tunneling and optical transitions is fully taken into account. From resulted lineshapes of the Fano resonance, we can evaluate tunneling rates of these metastable states and related absorption strengths relative to those of the continuum. The approach here is useful in estimations of carrier extraction rates from type-II nanostructures for photovoltaic applications.

OCIS codes: (160.4760) Optical properties; (040.4200) Multiple quantum well; (040.5350) Photovoltaic.

References and links

1. J. R. Meyer, C. L. Felix, W. W. Bewley, I. Vurgaftman, E. H. Aifer, L. J. Olafsen, J. R. Lindle, C. A. Hoffman, M.-J. Yang, B. R. Bennett, B. V. Shanabrook, H. Lee, C.-H. Lin, S. S. Pei, and R. H. Miles, "Auger coefficients in type-II InAs/Ga$_{1-x}$In$_x$Sb quantum wells," Appl. Phys. Lett. **73**, 2857–2859 (1998).
2. S. Kim, B. Fisher, H.-J. Eisler, and M. Bawendi, "Type-II quantum dots: CdTe/CdSe(core/shell) and CdSe/ZnTe(core/shell) heterostructures," J. Am. Chem. Soc. **125**, 11466–11467 (2003).
3. A. Ahland, D. Schulz, and E. Voges, "Accurate mesh truncation for Schrodinger equations by a perfectly matched layer absorber: Application to the calculation of optical spectra," Phys. Rev. B **60**, R5109–R5112 (1999).
4. J.-P. Berenger, "A perfectly matched layer for the absorption of electromagnetic waves," J. Comput. Phys. **114**, 185–200 (1994).
5. W. C. Chew and W. H. Weedon, "A 3D perfectly matched medium from modified Maxwell's equations with stretched coordinates," Microw. Opt. Technol. Lett. **7**, 599–604 (1994).
6. F. L. Teixeira and W. C. Chew, "General closed-form PML constitutive tensors to match arbitrary bianisotropic and dispersive linear media," IEEE Microw. Guided Wave Lett. **8**, 223–225 (1998).
7. S. Odermatt, M. Luisier, and B. Witzigmann, "Bandstructure calculation using the $k \cdot p$ method for arbitrary potentials with open boundary conditions," J. Appl. Phys. **97**, 046104 (2005).
8. M. Karner, A. Gehring, and H. Kosina, "Efficient calculation of lifetime based direct tunneling through stacked dielectrics," J. Comput. Electron. **5**, 161–165 (2006).
9. A. Ahland, M. Wiedenhaus, D. Schulz, and E. Voges, "Calculation of exciton absorption in arbitrary layered semiconductor nanostructures with exact treatment of the coulomb singularity," IEEE J. Quantum Electron. **36**, 842–848 (2000).
10. T.-Y. Zhang and W. Zhao, "Magnetoexcitonic optical absorption in semiconductors under strong magnetic fields and intense terahertz radiation in the Voigt configuration," EPL **82**, 67001 (2008).
11. U. Fano, "Effects of configuration interaction on intensities and phase shifts," Phys. Rev. **124**, 1866–1878 (1961).
12. S.-L. Chuang, S. Schmitt-Rink, D. A. B. Miller, and D. S. Chemla, "Exciton Green's-function approach to optical absorption in a quantum well with an applied electric field," Phys. Rev. B **43**, 1500–1509 (1991).

13. S. Glutsch, D. S. Chemla, and F. Bechstedt, "Numerical calculation of the optical absorption in semiconductor quantum structures," Phys. Rev. B **54**, 11592–11601 (1996).
14. J. M. Luttinger and W. Kohn, "Motion of electrons and holes in perturbed periodic fields," Phys. Rev. **97**, 869–883 (1955).
15. C. Y.-P. Chao and S. L. Chuang, "Spin-orbit-coupling effects on the valence-band structure of strained semiconductor quantum wells," Phys. Rev. B **46**, 4110–4122 (1992).
16. G. Liu and S.-L. Chuang, "Modeling of Sb-based type-II quantum cascade lasers," Phys. Rev. B **65**, 165220 (2002).
17. P.-F. Qiao, S. Mou, and S. L. Chuang, "Electronic band structures and optical properties of type-II superlattice photodetectors with interfacial effect," Opt. Express **20**, 2319–2334 (2012).
18. S. L. Chuang, *Physics of Photonic Devices*, 2nd ed. (John Wiley & Sons, New Jersey, 2009).
19. G. L. Bir and G. E. Pikus, *Symmetry and Strain-Induced Effects in Semiconductors* (John Wiley & Sons, New York, 1974).
20. G. D. Mahan, *Many-particle Physics*, 3rd ed. (Kluwer Academic/Plenum Publishers, New York, 2000).
21. S. L. Chuang, *Physics of Optoelectronic Devices* (John Wiley & Sons, New York, 1995).
22. C.-S. Chang and S. L. Chuang, "Modeling of strained quantum-well lasers with spin-orbit coupling," IEEE J. Sel. Topics Quantum Electron. **1**, 218–229 (1995).
23. S. L. Chuang and C. S. Chang, "A band-structure model of strained quantum-well wurtzite semiconductors," Semicond. Sci. Technol. **12**, 252–263 (1997).
24. D. Ahn and S.-L. Chuang, "Optical gain in a strained-layer quantum-well laser," IEEE J. Quantum Electron. **24**, 2400–2406 (1988).
25. F. Szmulowicz, "Derivation of a general expression for the momentum matrix elements within the envelope-function approximation," Phys. Rev. B **51**, 1613–1623 (1995).
26. Y.-C. Chang and R. B. James, "Saturation of intersubband transitions in p-type semiconductor quantum wells," Phys. Rev. B **39**, 12672–12681 (1989).
27. P. Lawaetz, "Valence-band parameters in cubic semiconductors," Phys. Rev. B **4**, 3460–3467 (1971).
28. X. Cartoixa, D. Z.-Y. Ting, and T. C. McGill, "Numerical spurious solutions in the effective mass approximation," J. Appl. Phys. **93**, 3974–3981 (2003).
29. G. B. Liu, S.-L. Chuang, and S.-H. Park, "Optical gain of strained GaAsSb/GaAs quantum-well lasers: A self-consistent approach," J. Appl. Phys. **88**, 5554–5561 (2000).
30. Y. Tsou, A. Ichii, and E. M. Garmire, "Improving InAs double heterostructure lasers with better confinement," IEEE J. Quantum Electron. **28**, 1261–1268 (1992).
31. P. K. W. Vinsome and D. Richardson, "The dielectric function in zincblende semiconductors," J. Phys. C: Solid St. Phys. **4**, 2650–2657 (1971).
32. C. G. Van de Walle, "Band lineups and deformation potentials in the model-solid theory," Phys. Rev. B **39**, 1871–1883 (1989).
33. R. E. Nahory, M. A. Pollack, J. C. DeWinter, and K. M. Williams, "Growth and properties of liquid-phase epitaxial GaAs$_{1-x}$Sb$_x$," J. Appl. Phys. **48**, 1607–1614 (1977).
34. D. Ahn, S. L. Chuang, and Y.-C. Chang, "Valence-band mixing effects on the gain and the refractive index change of quantum-well lasers," J. Appl. Phys. **64**, 4056–4064 (1988).

1. Introduction

The optical transitions in type-II semiconductor nanostructures are spatially indirect due to staggered alignments of conduction-band minima and valence-band maxima. Since electrons and holes are separated from each other, their wave-function overlaps are smaller than their type-I counterparts. This effect reduces various transition rates, both radiative and nonradiative, in type-II structures. Although the weaker absorption and emission in these nanostructures do make photon conversions less efficient in device applications, the lower nonradiative recombination rate is beneficial in other aspects. For example, the Auger recombination that is common in narrow-bandgap semiconductors is lower in type-II nanostructures than in their type-I counterparts [1, 2].

In addition to electron-hole separations, carriers are not necessarily tightly bound to nanostructures in type-II cases. Regions that are barriers for one type of carriers may be free spaces for those of the other type. For unconfined carriers, there may not be true bound states, but so-called quasi-bound states that appear as energy resonances of nanostructures may be present. Physically, carriers in the corresponding metastable states are initially generated near nanostructures but ultimately leave there. If this process is fast, the carriers in these states can be rapidly trans-

ferred to some separated channels/contacts before the (non)radiative recombination in nanostructures takes place. In this way, with some designs, the absorption of type-II nanostructures can be enhanced while the influence of nonradiative recombination remains mild.

The absorption of semiconductor nanostructures can be estimated with a few quantum-mechanical formalisms. These methods, nevertheless, presume that all the final states including unbound ones in an *infinite domain* containing the nanostructure are known. The domain size which ideally approaches infinity is crucial. In this limit, quantization conditions of states such as standing-wave and periodic boundary conditions (BCs) at outer domain boundaries should not affect responses around nanostructures. However, practical computations are carried out in finite domains. If domain sizes are not sufficiently large, the artificial quantization due to domain truncations can interfere with intrinsic quantum-mechanical features [3]. This phenomenon is unwanted if the original lineshapes do reflect some physics or dynamics. On the other hand, perfectly matched layers (PMLs) are commonly implemented in computations of electromagnetism to avoid unwanted reflections from outer domain boundaries [4–6]. In other words, these layers approximate the outgoing-wave BC and play the role of open spaces. They have also been adopted in calculations of electronic tunneling rates (imaginary parts of complex eigenenergies) for resonant tunneling diodes [7] and metal-oxide-semiconductor junctions [8], from which carriers escape without returning. In addition, these setups were utilized in the (magneto-) excitonic absorption within the two-band model [3, 9, 10]. Comparisons between cases with/without PMLs do show their essences [3]. Since PMLs model open spaces well, they can be a solution to domain truncations and keep the computation domain compact.

In this work, we generalize the aforementioned applications of PMLs to the bound-to-continuum absorption of type-II coupled quantum wells (QWs) with characteristics of tunneling inherent in quasi-bound states taken into account. Optical transitions of carriers from valence to conduction states are coherently interfered with the tunneling through conduction barriers. This effect results in various Fano resonances [11], of which their magnitudes determine absorption strengths, and spectral widths and skewness of their lineshapes reflect tunneling rates (coupling strengths) and interferences between the absorptions corresponding to metastable and continuum states. Unlike electronic cases [7, 8], the absorption and tunneling are not separable now and need to be considered simultaneously.

We convert evaluations of the absorption into a source-response problem [12, 13] through the Green functions of the eight-band Luttinger-Kohn (LK) Hamiltonian [14–18] corrected by Bir-Pikus (BP) strain terms [19]. Here, the source in this eight-band space is related to the momentum operation of initial states in bound valence subbands. While various Green functions with different BCs may be utilized [20], we adopt the *retarded* one, which is motivated by the effective outgoing-wave BC of PMLs, namely, sources *radiate* in the eight-band space. In this way, we do not really solve the quasi-bound states but setup their presence through PMLs. In fact, neither do we construct the retarded Green function of the eight-band Hamiltonian due to its cumbersomeness. Rather, we directly tackle the problem by computing the source-generated field, which is governed by the wave equation of the eight-band Hamiltonian with band mixing.

The remaining of this paper is organized as follows. In section 2, we first introduce the eight-band effective Hamiltonian [16] as applied to type-II coupled QWs. Then, we begin from the density-matrix formalism and convert the bound-to-continuum photon absorption in the presence of quantum tunneling into an effective source-radiation problem in the eight-band space of this Hamiltonian. The inclusion of PMLs is presented afterward. In section 3, we apply this approach to type-II coupled QWs based on the gallium-arsenide-antimony (GaAsSb) material system and utilize characteristics of the Fano lineshape to extract tunneling lifetimes of the metastable states and their absorption magnitudes relative to those of the continuum (the Fano parameter). A conclusion is given in section 4, and technical details are left in appendices.

2. Theoretical formulation

2.1. Eight-band effective Hamiltonian

The $\mathbf{k} \cdot \mathbf{p}$ method is a technique for the bandstructure calculations of semiconductor bulks and nanostructures near the Brillouin zone (BZ) center. The eight-band LK Hamiltonian corrected by BP strain terms is a variant of the technique. In this scheme, two conduction and six valence bands are considered. The six valence bands include two heavy-hole (HH), two light-hole (LH), and two spin-orbit split-off (SO) bands. In addition, the spin-orbit coupling, corrections from other bands (Loẅdin's perturbations up to the second order in the wave vector $\mathbf{k}$) [16, 21], and strain effect are incorporated in this method. Details on Bloch parts $|u_l\rangle$ of these bands at the BZ center and matrix elements $H_{l'l}[\mathbf{k}]$ of the eight-band Hamiltonian in bulk semiconductors ($l, l' = 1 - 8$ for two conduction and six valence bands) are presented in appendix A.

In semiconductor QWs, the position ($\mathbf{r}$) representation $\Psi^{(n,\mathbf{k_t})}(\mathbf{r})$ of state $|n, \mathbf{k_t}\rangle$ is approximated in the eight-band space as

$$\Psi^{(n,\mathbf{k_t})}(\mathbf{r}) = \langle \mathbf{r}|n, \mathbf{k_t}\rangle \simeq \frac{e^{i\mathbf{k_t}\cdot\boldsymbol{\rho}}}{\sqrt{A_{QW}}} \sum_{l=1}^{8} \phi_l^{(n,\mathbf{k_t})}(z) u_l(\mathbf{r}), \tag{1}$$

where n is the subband label which may indicate the unbound continuum; $\mathbf{k_t}$ is the wave vector transverse to the growth direction z ([001] crystal axis); $\boldsymbol{\rho}$ is the transverse coordinate; A_{QW} is the QW area; $\phi_l^{(n,\mathbf{k_t})}(z)$ is the envelop function of band l; and $u_l(\mathbf{r})$ are position representations of Bloch parts $|u_l\rangle$. If subband n is a bound one, the envelop functions $\phi_l^{(n,\mathbf{k_t})}(z)$ can be properly normalized as $\sum_l \int dz |\phi_l^{(n,\mathbf{k_t})}(z)|^2 = 1$. On the other hand, the normalization of unbound subbands may depend on n in a nontrivial way. Utilizations of the Green function would, however, resolve the issue.

We first turn the Hamiltonian matrix elements $H_{l'l}[\mathbf{k}]$ of bulk semiconductors into real-space operators, from which we construct the Schrodinger's equation of envelop functions $\phi_l^{(n,\mathbf{k_t})}(z)$ under the multiband effective-mass approximation as

$$\sum_{l=1}^{8} H_{l'l}\left[\mathbf{k_t}, k_z = -i\partial_z\right] \phi_l^{(n,\mathbf{k_t})}(z) = E_{n,\mathbf{k_t}} \phi_{l'}^{(n,\mathbf{k_t})}(z), \tag{2}$$

where the wave-vector component k_z is replaced with the differential operator $-i\partial_z \equiv -i\partial/\partial z$; and $E_{n,\mathbf{k_t}}$ is the eigenenergy of state $|n, \mathbf{k_t}\rangle$ and may depend on label n in a continuous fashion for unbound subbands. In Eq. (2), whenever the operator $-i\partial_z$ and a spatial function appear together in $H_{l'l}[\mathbf{k_t}, k_z = -i\partial_z]$, the hermitian forms are adopted:

$$A(z)[-i\partial_z]^2 \rightarrow -\partial_z A(z)\partial_z, \quad B(z)[-i\partial_z] \rightarrow -\frac{i}{2}\left[B(z)\partial_z + \partial_z B(z)\right], \tag{3}$$

where $A(z)$ and $B(z)$ are some spatial functions of z.

The multiband Schrodinger's equation in Eq. (2) is an eigenvalue problem. For bound subbands, we adopt the finite-difference (FD) method to solve envelop functions $\phi_{l'}^{(n,\mathbf{k_t})}(z)$ and energies $E_{n,\mathbf{k_t}}$ [22, 23]. For unbound ones, no calculations of envelop functions and energies would be carried out, but the FD scheme is still utilized in the equivalent source-radiation approach to be described in section 2.2. In addition, if the anisotropy of bandstructures is minor, namely, $E_{n,\mathbf{k_t}}$ mostly depends on the magnitude k_t of transverse wave vector $\mathbf{k_t}$ rather than on its direction, the axial approximation is often adopted [15, 16]. After some basis transformations, this approximation block-diagonalizes the eight-band Hamiltonian into two four-band ones. Note that the new eigenenergies and envelop functions of the two four-band Hamiltonians only

depend on k_t, and the directional dependence of calculations on $\mathbf{k}_t$ can be simplified or removed in this way. The property reduces the amount of computations significantly but does not alter the tunneling effect much. Therefore, this approximation is applied here. Details on the axial approximation are presented in appendix B.

2.2. Source-radiation approach to photon absorption

From the density-matrix formalism, the relative permittivity tensor $\varepsilon_{r,ij}(\omega)$ ($i,j = x,y,z$) at a frequency ω corresponding to bound-to-continuum transitions with negligible photon momenta ($\mathbf{k}$ selection rules) can be expressed as [21, 24]

$$\varepsilon_{r,ij}(\omega) = \varepsilon_{r,b,ij}(\omega) + \frac{1}{\varepsilon_0 V_{QW}} \sum_{\mathbf{k}_t} \sum_{n,n'}{}' \left(f_{n,\mathbf{k}_t} - f_{n',\mathbf{k}_t} \right)$$
$$\times \left(\frac{e}{m_0 \omega} \right)^2 \left(\frac{p^i_{nn',\mathbf{k}_t} p^j_{n'n,\mathbf{k}_t}}{E_{n'n,\mathbf{k}_t} - \hbar\omega - i\Upsilon_{\mathbf{k}_t}} + \frac{p^j_{nn',\mathbf{k}_t} p^i_{n'n,\mathbf{k}_t}}{E_{n'n,\mathbf{k}_t} + \hbar\omega + i\Upsilon_{\mathbf{k}_t}} \right), \tag{4}$$

where $\varepsilon_{r,b,ij}(\omega)$ is the relative background permittivity; ε_0 is the vacuum permittivity; V_{QW} is the volume of coupled QWs and is set to $A_{QW}h_{QW}$ with h_{QW} being the total thickness of coupled QWs; e and m_0 are the charge and mass of free electrons, respectively; $\hbar$ is Planck constant; n is the label of *bound* valence subbands while n' is that of final subbands including quasi-bound ones in conduction bands; $p^j_{n'n,\mathbf{k}_t} = \langle n', \mathbf{k}_t | p_j | n, \mathbf{k}_t \rangle$ is the matrix element of the momentum operator p_j in direction j ($j = x,y,z$); $E_{n'n,\mathbf{k}_t}$ is the energy difference $E_{n',\mathbf{k}_t} - E_{n,\mathbf{k}_t}$; $\Upsilon_{\mathbf{k}_t}$ is the half width at half maximum (HWHM) of the transition due to various relaxation and dephasing mechanisms for states at $\mathbf{k}_t$; $f_{n,\mathbf{k}_t}$ and $f_{n',\mathbf{k}_t}$ are occupation numbers of the corresponding states and are modeled as the Fermi-Dirac distribution $f_{FD}(E) = \{\exp[(E - E_F)/(k_B T)] + 1\}^{-1}$ with the Fermi energy E_F and thermal energy $k_B T$; and the prime (') after the summation over n and n' means that only subband pairs (n,n') with $E_{n',\mathbf{k}_t} > E_{n,\mathbf{k}_t}$ are considered.

For most of the cases in which the time-reversal symmetry of quantum states is unbroken (absence of the magnetism or external magnetic field), the permittivity tensors $\varepsilon_{r,ij}(\omega)$ and $\varepsilon_{r,b,ij}(\omega)$ are symmetric with respect to indices i and j. Under such circumstances, we can rewrite $\varepsilon_{r,ij}(\omega) = [\varepsilon_{r,ij}(\omega) + \varepsilon_{r,ji}(\omega)]/2$ as

$$\varepsilon_{r,ij}(\omega) = \varepsilon_{r,b,ij}(\omega) + \frac{1}{\varepsilon_0 V_{QW}} \sum_{\mathbf{k}_t,n} X_{n,\mathbf{k}_t,ij}(\omega), \tag{5a}$$

$$X_{n,\mathbf{k}_t,ij}(\omega) = \left(\frac{e}{m_0 \omega} \right)^2 \sum_{n'}{}' \frac{1}{2} \left(f_{n,\mathbf{k}_t} - f_{n',\mathbf{k}_t} \right) \left(p^i_{nn',\mathbf{k}_t} p^j_{n'n,\mathbf{k}_t} + p^j_{nn',\mathbf{k}_t} p^i_{n'n,\mathbf{k}_t} \right)$$
$$\times \left(\frac{1}{E_{n'n,\mathbf{k}_t} - \hbar\omega - i\Upsilon_{\mathbf{k}_t}} + \frac{1}{E_{n'n,\mathbf{k}_t} + \hbar\omega + i\Upsilon_{\mathbf{k}_t}} \right). \tag{5b}$$

The imaginary part of the function $X_{n,\mathbf{k}_t,ij}$ is directly related to the polarized absorption $\alpha_i(\omega) = 2(\omega/c)\text{Im}\left[\sqrt{\varepsilon_{r,ii}(\omega)} \right]$ ($i = x,y,z$) and is further approximated as [21]

$$\alpha_i(\omega) \approx \frac{1}{\sqrt{\text{Re}\left[\varepsilon_{r,b,ii}(\omega)\right]}} \left(\frac{\omega}{c} \right) \left\{ \text{Im}\left[\varepsilon_{r,b,ii}(\omega)\right] + \frac{1}{\varepsilon_0 V_{QW}} \sum_{\mathbf{k}_t,n} \text{Im}\left[X_{n,\mathbf{k}_t,ii}(\omega)\right] \right\}. \tag{6}$$

In Eq. (6), we obtain the transverse-electric (TE) and transverse-magnetic (TM) absorption spectra if i is set to x (y) and z, respectively. After taking the imaginary part of $X_{n,\mathbf{k}_t,ij}(\omega)$, we turn the content inside the last parentheses of Eq. (5b) into two Lorentzians. In this way, we

may alternatively express $\mathrm{Im}[X_{n,\mathbf{k}_\mathrm{t},ij}(\omega)]$ as

$$\mathrm{Im}\left[X_{n,\mathbf{k}_\mathrm{t},ij}(\omega)\right] = \left(\frac{e}{m_0\omega}\right)^2 \left[I_{n,\mathbf{k}_\mathrm{t},ij}(\omega) - I_{n,\mathbf{k}_\mathrm{t},ij}(-\omega)\right], \tag{7a}$$

$$I_{n,\mathbf{k}_\mathrm{t},ij}(\omega) = \int_0^\infty d\omega' \frac{1}{\pi} \frac{\Upsilon_{\mathbf{k}_\mathrm{t}}/\hbar}{[(\omega - \omega')^2 + (\Upsilon_{\mathbf{k}_\mathrm{t}}/\hbar)^2]} \mathrm{Im}\left[V_{n,\mathbf{k}_\mathrm{t},ij}(\omega') + V_{n,\mathbf{k}_\mathrm{t},ji}(\omega')\right], \tag{7b}$$

$$V_{n,\mathbf{k}_\mathrm{t},ij}(\omega') = \frac{1}{2}\left[f_{\mathrm{FD}}(E_{n,\mathbf{k}_\mathrm{t}}) - f_{\mathrm{FD}}(E_{n,\mathbf{k}_\mathrm{t}} + \hbar\omega')\right] \sum_{n'} \frac{p^i_{nn',\mathbf{k}_\mathrm{t}} p^j_{n'n,\mathbf{k}_\mathrm{t}}}{E_{n',\mathbf{k}_\mathrm{t}} - (E_{n,\mathbf{k}_\mathrm{t}} + \hbar\omega') - i\eta}, \tag{7c}$$

where $\eta = 0^+$ is an infinitesimal positive number; and we no longer constrain the summation over n' in Eq. (7c) with the condition $E_{n',\mathbf{k}_\mathrm{t}} > E_{n,\mathbf{k}_\mathrm{t}}$ because the integration in Eq. (7b) is only performed at $\omega' > 0$. Calculations of polarized absorption spectra $\alpha_i(\omega)$ for type-II coupled QWs are now simplified to evaluations of the function $V_{n,\mathbf{k}_\mathrm{t},ij}(\omega')$ which solely reflects intrinsic features of the initial and final states other than broadenings ($\Upsilon_{\mathbf{k}_\mathrm{t}}$).

The band mixing effect needs to be taken into account in the evaluations of momentum matrix elements in the eight-band space. Analogous to the $\mathbf{k}\cdot\mathbf{p}$ method, matrix elements of the eight-band Hamiltonian may be written as $H_{l'l}[\mathbf{k}] \simeq H_{l'l}[\mathbf{0}] + (\hbar/m_0)\mathbf{k}\cdot\mathbf{p}_{l'l}[\mathbf{k}=\mathbf{0}] + O(k_i k_j)$. Further generalizing this analogy, we express the momentum matrix elements of bulk semiconductors in the eight-band space as [17, 25]

$$\mathbf{p}_{l'l}[\mathbf{k}] = \frac{m_0}{\hbar}\nabla_\mathbf{k} H_{l'l}[\mathbf{k}] = \mathbf{\Gamma}_{l'l} + \hbar k_z \mathbf{Q}_{l'l} + \hbar\mathbf{\Lambda}_{l'l}[\mathbf{k}_\mathrm{t}], \tag{8}$$

where $\mathbf{\Gamma}_{l'l}$, $\mathbf{Q}_{l'l}$, and $\mathbf{\Lambda}_{l'l}[\mathbf{k}_\mathrm{t}]$ are matrix elements derived from $H_{l'l}[\mathbf{k}]$. The expressions of these matrices are shown in appendix C. For nanostructres, we replace $\mathbf{p}_{l'l}[\mathbf{k}]$ with real-space operators $\mathbf{p}_{l'l}[\mathbf{k}_\mathrm{t}, k_z = -i\partial_z]$ and calculate momentum matrix elements $p^j_{n'n,\mathbf{k}_\mathrm{t}}$ ($j = x,y,z$) with the hermitian form in Eq. (3) and envelop functions as follows [17, 25, 26]:

$$p^j_{n'n,\mathbf{k}_\mathrm{t}} = \langle n', \mathbf{k}_\mathrm{t}|p_j|n,\mathbf{k}_\mathrm{t}\rangle = \sum_{l',l}\int_{-\infty}^\infty dz \phi_{l'}^{(n',\mathbf{k}_\mathrm{t})*}(z) p_{j,l'l}[\mathbf{k}_\mathrm{t}, k_z = -i\partial_z]\phi_l^{(n,\mathbf{k}_\mathrm{t})}(z)$$

$$\equiv \sum_{l'}\int_{-\infty}^\infty dz \phi_{l'}^{(n',\mathbf{k}_\mathrm{t})*}(z) J_{j,l'}^{(n,\mathbf{k}_\mathrm{t})}(z), \tag{9}$$

where $p_{j,l'l}[\mathbf{k}_\mathrm{t}, k_z = -i\partial_z] = \hat{j}\cdot\mathbf{p}_{l'l}[\mathbf{k}_\mathrm{t}, k_z = -i\partial_z]$ ($j = x,y,z$); and a new field $J_{j,l'}^{(n,\mathbf{k}_\mathrm{t})}(z)$ resulted from the momentum operation is defined as

$$J_{j,l'}^{(n,\mathbf{k}_\mathrm{t})}(z) \equiv \sum_l p_{j,l'l}[\mathbf{k}_\mathrm{t}, k_z = -i\partial_z]\phi_l^{(n,\mathbf{k}_\mathrm{t})}(z)$$

$$= \sum_l \left\{ \Gamma_{j,l'l}(z)\phi_l^{(n,\mathbf{k}_\mathrm{t})}(z) - \frac{i\hbar}{2}\left(Q_{j,l'l}(z)\partial_z[\phi_l^{(n,\mathbf{k}_\mathrm{t})}(z)] + \partial_z\left[Q_{j,l'l}(z)\phi_l^{(n,\mathbf{k}_\mathrm{t})}(z)\right]\right) \right.$$

$$\left. + \hbar\Lambda_{j,l'l}[\mathbf{k}_\mathrm{t}, z]\phi_l^{(n,\mathbf{k}_\mathrm{t})}(z) \right\}. \tag{10}$$

In Eq. (10), $\Gamma_{j,l'l}(z)$, $Q_{j,l'l}(z)$, and $\Lambda_{j,l'l}[\mathbf{k}_\mathrm{t}, z]$ are the j component ($j = x,y,z$) of the matrix elements $\mathbf{\Gamma}_{l'l}(z)$, $\mathbf{Q}_{l'l}(z)$, and $\mathbf{\Lambda}_{l'l}[\mathbf{k}_\mathrm{t}, z]$, respectively, and we have included the position dependence (z) in their arguments due to the presence of coupled QWs.

Using the integral form of matrix element $p^j_{n'n,\mathbf{k}_\mathrm{t}}$ in Eq. (9), we rewrite function $V_{n,\mathbf{k}_\mathrm{t},ij}(\omega')$

in Eq. (7c) as

$$V_{n,\mathbf{k}_t,ij}(\omega') = \frac{1}{2}\left[f_{\mathrm{FD}}(E_{n,\mathbf{k}_t}) - f_{\mathrm{FD}}(E_{n,\mathbf{k}_t} + \hbar\omega')\right]$$
$$\times \sum_{l,l'}\int_{-\infty}^{\infty}\mathrm{d}z\int_{-\infty}^{\infty}\mathrm{d}z' J_{i,l}^{(n,\mathbf{k}_t)*}(z)G_{\mathbf{k}_t,ll'}^{(\mathrm{R})}(z,z',E_{n,\mathbf{k}_t}+\hbar\omega')J_{j,l'}^{(n,\mathbf{k}_t)}(z'), \qquad (11)$$

where the retarded Green function $G_{\mathbf{k}_t,ll'}^{(\mathrm{R})}(z,z',E)$ in the eight-band space is

$$G_{\mathbf{k}_t,ll'}^{(\mathrm{R})}(z,z',E) = \sum_{n'}\frac{\phi_l^{(n',\mathbf{k}_t)}(z)\phi_{l'}^{(n',\mathbf{k}_t)*}(z')}{E_{n',\mathbf{k}_t} - E - i\eta}. \qquad (12)$$

We further construct a field $F_{j,l}^{(n,\mathbf{k}_t)}(z,\omega')$ from $J_{j,l'}^{(n,\mathbf{k}_t)}(z)$ and this Green function through a response integral:

$$F_{j,l}^{(n,\mathbf{k}_t)}(z,\omega') = \sum_{l'}\int_{-\infty}^{\infty}\mathrm{d}z' G_{\mathbf{k}_t,ll'}^{(\mathrm{R})}(z,z',E_{n,\mathbf{k}_t}+\hbar\omega')J_{j,l'}^{(n,\mathbf{k}_t)}(z'), \qquad (13)$$

with which we reorganize $V_{n,\mathbf{k}_t,ij}(\omega')$ in Eq. (11) as

$$V_{n,\mathbf{k}_t,ij}(\omega') = \frac{1}{2}\left[f_{\mathrm{FD}}(E_{n,\mathbf{k}_t}) - f_{\mathrm{FD}}(E_{n,\mathbf{k}_t}+\hbar\omega')\right]\sum_l\int_{-\infty}^{\infty}\mathrm{d}z J_{i,l}^{(n,\mathbf{k}_t)*}(z)F_{j,l}^{(n,\mathbf{k}_t)}(z,\omega'). \qquad (14)$$

Analogous to cases in electromagnetism, the summation of various spatial integrals over l in Eq. (14) resembles the complex source-generated power density $-\mathbf{J}_s^*(\mathbf{r})\cdot\mathbf{E}(\mathbf{r})$ in Poynting's theorem, where $\mathbf{J}_s(\mathbf{r})$ and $\mathbf{E}(\mathbf{r})$ are the source and electric field, respectively. Furthermore, the radiation field $\mathbf{E}(\mathbf{r})$ is connected to the source $\mathbf{J}_s(\mathbf{r})$ through a dyadic Green function, which is similar to the relation between $F_{j,l}^{(n,\mathbf{k}_t)}(z,\omega')$ and $J_{j,l}^{(n,\mathbf{k}_t)}(z)$ in Eq. (13). From this viewpoint, we have converted calculations of absorption spectra into an equivalent source-radiation problem in the eight-band space of the effective Hamiltonian.

Rather than working on the wave functions of quasi-bound states which are not properly solved under the truncation of computation domains, we disguise them into the retarded Green function. However, neither do we explicitly construct this Green function in the eight-band space due to its cumbersomeness. In fact, we solve $F_{j,l}^{(n,\mathbf{k}_t)}(z,\omega')$ through the differential equation of the eight-band effective Hamiltonian. The retarded Green function is the inverse operator of the eight-band effective Hamiltonian up to a (complex) energy shift, namely,

$$\sum_{l=1}^{8}\left\{H_{\tilde{l}l}[\mathbf{k}_t,k_z=-i\partial_z] - (E+i\eta)\delta_{\tilde{l}l}\right\}G_{\mathbf{k}_t,ll'}^{(\mathrm{R})}(z,z',E) = \delta_{\tilde{l}l'}\delta(z-z'), \qquad (15)$$

where the presence of Kronecker delta $\delta_{\tilde{l}l'}$ and Dirac delta function $\delta(z-z')$ is due to the completeness relation of envelop functions $\phi_l^{(n',\mathbf{k}_t)}(z)$: $\sum_{n'}\phi_l^{(n',\mathbf{k}_t)}(z)\phi_{l'}^{(n',\mathbf{k}_t)*}(z') = \delta_{ll'}\delta(z-z')$. This relation directly incorporates the normalization of various states, including bound and quasi-bound ones, into the retarded Green function. Utilizing Eqs. (13) and (15), one can show that the field $F_{j,l}^{(n,\mathbf{k}_t)}(z,\omega')$ is the solution of the following differential equation:

$$\sum_{l=1}^{8}\left\{H_{\tilde{l}l}[\mathbf{k}_t,k_z=-i\partial_z] - (E_{n,\mathbf{k}_t}+\hbar\omega'+i\eta)\delta_{\tilde{l}l}\right\}F_{j,l}^{(n,\mathbf{k}_t)}(z,\omega') = J_{j,\tilde{l}}^{(n,\mathbf{k}_t)}(z). \qquad (16)$$

Equation (16) indicates that the response $F_{j,l}^{(n,\mathbf{k}_t)}(z,\omega')$ is generated by the source $J_{j,l}^{(n,\mathbf{k}_t)}(z)$, namely, a source-radiation problem in the eight-band space. The field $F_{j,l}^{(n,\mathbf{k}_t)}(z,\omega')$ can be directly solved from Eq. (16) rather than Eq. (13), where the retarded Green function is used.
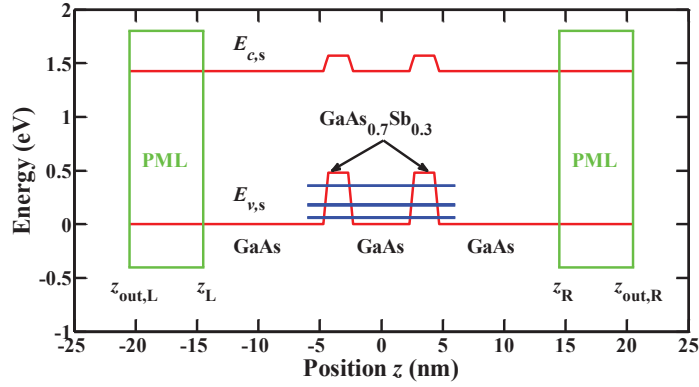
Fig. 1. The band diagram of type-II GaAs$_{0.7}$Sb$_{0.3}$ coupled QWs. The strained conduction bandedge $E_{c,s}$ and valence counterpart $E_{v,s}$ are marked in red lines. The blue lines indicate energies of a few bound valence subbands at the BZ center. The PMLs (green regions) at two ends of the computation domain effectively model the open regions.

2.3. Perfectly-matched layers in eight-band space

Since we adopt the retarded Green function in the formulation, the causality requires generated fields due to localized sources to be outgoing at $z \to \pm\infty$. Numerically, the outgoing-wave BC has to be imposed on the response field $F_{j,l}^{(n,\mathbf{k}_t)}(z, \omega')$. To realize this BC in finite computation domains, we apply PMLs to the source-radiation problem in section 2.2.

In Maxwell's equations, PMLs are often introduced through the complex-stretched coordinate [5, 6]. They are present at rims of computation domains as some effective media which absorb outgoing waves and avoid reflections there [4]. As shown in Fig. 1, for the type-II GaAs$_{0.7}$Sb$_{0.3}$ coupled QWs to be considered in section 3, we can also apply this concept to the differential equation in Eq. (16) and locate the corresponding effective media at two ends of the computation domain [7]. We adopt the complex-stretched coordinate $z_s(z)$ as follows:

$$z_s(z) = z + iz_I(z) = \begin{cases} z - i\kappa \left(\frac{z_L - z}{h_z} \right)^m, & z_{\text{out},L} < z < z_L, \\ z, & z_L < z < z_R, \\ z + i\kappa \left(\frac{z - z_R}{h_z} \right)^m, & z_R < z < z_{\text{out},R}, \end{cases} \tag{17}$$

where z_L and z_R are the left and right boundaries at which the central computation domain contacts the left and right PMLs, respectively; $z_{\text{out},L}$ ($z_{\text{out},R}$) is the leftmost (rightmost) boundary of the whole computation domain; m (≥ 1) indicates the order of complex-stretched coordinates in PMLs; and h_z and κ are some length scales. In accordance to the definition of the complex-stretched coordinate in Eq. (17), the corresponding partial derivative with z_s is related to that with the real-space one (z) as $\partial_{z_s} = \partial/\partial z_s = [s_z(z)]^{-1}\partial_z$, where the stretching parameter $s_z(z)$ is defined as $s_z(z) = \partial z_s(z)/\partial z$ [7]. We note that outgoing waves $\exp(\pm ik_z z_s)$ propagating along $\pm z$ directions become exponentially decreasing toward $z \to \pm\infty$ with the factor $\exp[-k_z|z_I(z)|]$ once they enter PMLs. If these PMLs are sufficiently thick, outgoing waves become exponentially small before they reach the outmost boundaries of the computation domain and virtually do not reflect back. Under such circumstances, results of calculations would be insensitive to the true BC at the outmost boundaries, and we can choose whatever BCs that are convenient for our numerical implementations, for example, the null Dirichlet (hard-wall) BC.

Suppose that in the space of z_s, the field $\hat{F}_{j,l}^{(n,\mathbf{k}_t)}(z_s, \omega')$ is generated by a finite-extent source

$\hat{J}_{j,\tilde{l}}^{(n,\mathbf{k}_t)}(z_s)$, namely, $\hat{F}_{j,l}^{(n,\mathbf{k}_t)}(z_s,\omega')$ is the solution to Eq. (16) in the presence of $\hat{J}_{j,\tilde{l}}^{(n,\mathbf{k}_t)}(z_s)$ as z is changed to z_s. We then carry out the transformation of $z_s(z)$ in Eq. (17) and write two resulted fields $F_{j,l}^{(n,\mathbf{k}_t,s)}(z,\omega')$ and $J_{j,\tilde{l}}^{(n,\mathbf{k}_t,s)}(z)$ in the real space of z as

$$F_{j,l}^{(n,\mathbf{k}_t,s)}(z,\omega') = \hat{F}_{j,l}^{(n,\mathbf{k}_t)}(z_s(z),\omega'), \quad J_{j,\tilde{l}}^{(n,\mathbf{k}_t,s)}(z) = \hat{J}_{j,\tilde{l}}^{(n,\mathbf{k}_t)}(z_s(z)), \qquad (18)$$

where the superscript "s" means that the fields originate from the space of z_s. The field $F_{j,l}^{(n,\mathbf{k}_t,s)}(z,\omega')$ and source $J_{j,\tilde{l}}^{(n,\mathbf{k}_t,s)}(z)$ satisfy the following differential equation in the real space:

$$\sum_{l=1}^{8} \left\{ H_{\tilde{l}l}\left[\mathbf{k}_t, k_{z_s} = -i[s_z(z)]^{-1}\partial_z\right] - (E_{n,\mathbf{k}_t} + \hbar\omega' + i\eta)\delta_{\tilde{l}l} \right\} F_{j,l}^{(n,\mathbf{k}_t,s)}(z,\omega') = J_{j,\tilde{l}}^{(n,\mathbf{k}_t,s)}(z), \quad (19)$$

where the effect of PMLs comes into play through the stretching parameter $s_z(z)$. Since the parameter $s_z(z)$ is unity in the central computation domain ($z_L < z < z_R$), the differential equation in Eq. (19) is identical to that in Eq. (16) in this region. Furthermore, if we set $J_{j,\tilde{l}}^{(n,\mathbf{k}_t,s)}(z)$ to the counterpart $J_{j,\tilde{l}}^{(n,\mathbf{k}_t)}(z)$ in Eq. (16) and assume that both sources are solely present in the central computation domain, the field $F_{j,l}^{(n,\mathbf{k}_t,s)}(z,\omega')$ there would resemble the very field $F_{j,l}^{(n,\mathbf{k}_t)}(z,\omega')$ in Eq. (16) that is radiated into free spaces. In this way, the integrand $J_{i,l}^{(n,\mathbf{k}_t)*}(z)F_{j,l}^{(n,\mathbf{k}_t)}(z,\omega')$ in Eq. (14) can be well approximated with $J_{i,l}^{(n,\mathbf{k}_t,s)*}(z)F_{j,l}^{(n,\mathbf{k}_t,s)}(z,\omega')$, which is then solely integrated in the central computation domain.

In practical computations, we impose the hard-wall BC on the envelop function of *bound* valence subbands n at boundaries $z = z_L$ and $z = z_R$. This setup does not significantly alter the properties regarding to bound subbands as long as the central computation domain is decently large. In addition, the penetration of $J_{j,\tilde{l}}^{(n,\mathbf{k}_t)}(z)$ into PMLs is avoided so that the aforementioned procedures are applicable. Numerically, we use the FD method to discretize Eq. (19) in the computation domain including PMLs. The resulted system of linear equations is then arranged in the matrix form and solved.

3. Results and discussions

As an example, we calculate the bound-to-continuum absorption spectra of $GaAs_{0.7}Sb_{0.3}/GaAs$ type-II coupled QWs under different widths of $GaAs_{0.7}Sb_{0.3}$ layers at room temperature. The features associated with the tunneling effect are also investigated and discussed. The axial approximation is adopted in calculations of bound valence subbands, which reduces the dependence on the full transverse wave vector $\mathbf{k}_t$ to that on its magnitude k_t. Details of this approximation are shown in appendix B. Here, it is sufficient to know that under the approximation, states can be further classified into two groups labeled by an index $\sigma = U, L$ indicating whether they originate from the upper (U) block-diagonal Hamiltonian matrix operator or lower (L) one. For states in subband n' from either group, they are represented by four envelop functions $\phi_v'^{(\sigma,n',k_t)}(z)$ [$v = 1 - 4$, and the superscript ($'$) means the joint space of two block-diagonal Hamiltonian matrix operators]. These four envelop functions consecutively characterize the conduction, HH, LH, and SO components.

The material parameters of GaAs and GaSb are listed in Table 1 [17, 18, 27–31]. Their presences in the eight-band Hamiltonian are shown in appendix A, and some related remarks are addressed here. The Luttinger parameters of GaAs [27] are chosen to avoid spurious solutions [28] in eight-band calculations, and valence-band offset (VBO) energies of the two materials are obtained from the model-solid theory [32] or empirical method [29, 30]. Linear interpolations

Table 1. Material parameters in eight-band calculations

Parameter	Symbol (unit)	GaAs [18, 27]	GaSb [17]
Lattice constant	a (Å)	5.6533	6.0854
Band gap at 300K	E_g (eV)	1.424	0.73 [29]
Spin-orbit split-off energy	Δ (eV)	0.34	0.81
Deformation potentials	a_c (eV)	−7.17	−7.5
	a_v (eV)	1.16	0.8
	b (eV)	−1.7	−2.0
Elastic stiffness constants	C_{11} (10^{11}ba)	11.879	8.842
	C_{12} (10^{11}ba)	5.376	4.026
Optical matrix parameter	E_p (eV)	25.7	22.4
Conduction effective mass	m_c (m_0)	0.0665	0.0412
Inverse of bare relative conduction effective mass	γ_c	1.0 [28]	1.0 [28]
Luttinger parameters [17, 27]	γ_1^L	7.65	11.84
	γ_2^L	2.41	4.25
	γ_3^L	3.28	5.01
Bare Luttinger parameters	γ_1	2.078	4.37
	γ_2	−0.376	0.52
	γ_3	0.494	1.28
Valence-band offset energy [29, 30]	VBO (eV)	0.48	1.16
Dielectric constant [18, 31]	$\varepsilon_{r,b}$	13.1	14.5

between the parameters of GaAs and GaSb are used to obtain those of GaAs$_{0.7}$Sb$_{0.3}$ except for the bandgap energy $E_g(x)$ and valence bandedge $E_v(x)$ at an antimony composition of $x = 0.3$, where the bowing parameters are set to -1.2 eV [29,33] and 1.08 eV (fitting to the experimental data) [29], respectively.

We first consider type-II coupled QWs composed of a 5 nm central GaAs region and two 2 nm GaAs$_{0.7}$Sb$_{0.3}$ layers. The free spaces, including PMLs, are modeled as two GaAs regions with a thickness of 16 nm outside the type-II nanostructure. The strained conduction bandedge $E_{c,s}$ and valence counterpart $E_{v,s}$ (red lines) as a function of position z near these coupled QWs are depicted in Fig. 1. The valence bandedge $E_{v,s}$ of bulk GaAs is set to 0 eV as a reference. The energies of these bound valence subbands at the BZ center are also marked (blue lines). The two GaAs$_{0.7}$Sb$_{0.3}$ layers play the role of QWs for valence electrons or holes, but the high conduction bandedges there turn them into barriers for conduction electrons. Unlike carriers in bound valence subbands, conduction electrons only tentatively stay in some metastable states of the central GaAs region but eventually leak out from the nanostructure.

In Fig. 2(a), we show bandstructures E_{n',k_t}^U of the bound valence subbands versus k_t. The spectrally dense valence subbands (black lines), of which the corresponding BZ centers are below the valence bandedge of bulk GaAs (0 eV), originate from the ideally unbound space. However, these subbands are significantly affected by the finite size of the computation domain, and the associated absorption would not be discussed here. For bound valence subbands, there are four HH-like (HH envelop functions dominate, blue lines) and two LH-like ones (LH counterparts dominate, red lines), and each of them is doubly degenerate (no splittings between two groups of states labeled by $\sigma = U, L$). The first two HH-like subbands (HH1 and HH2) are close in energies. Figures 2(b) and 2(c) show the envelope functions $\phi_v'^{(U,n',k_t)}(z)$ ($v = 1 - 4$) at $k_t = 0$ for the first and third bound valence subbands ($n' = 1, 3$). All these envelop functions can be set real. At the BZ center, due to a nanostructure with the inversion symmetry, the envelop
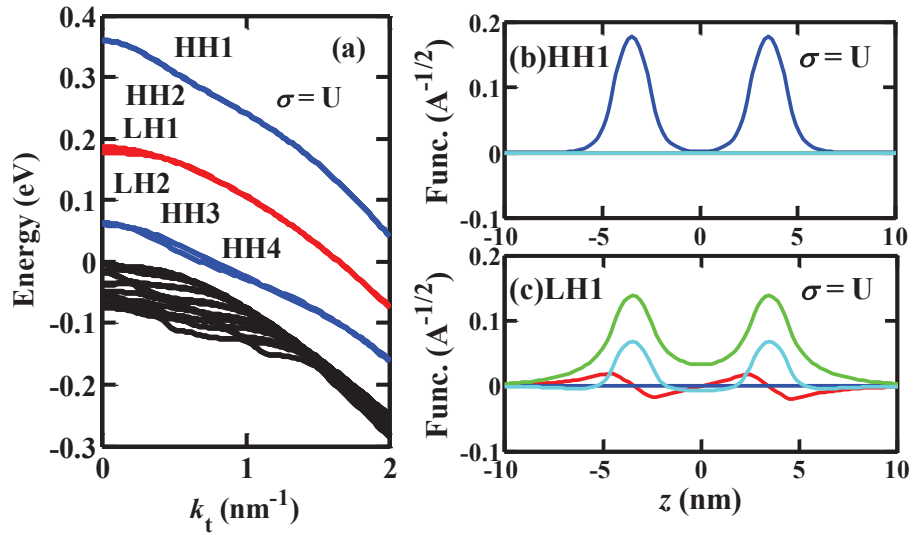
Fig. 2. (a) The valence subband structures E_{n',k_t}^U versus k_t. There are six bound subbands which are doubly degenerate. Four of them are HH-like (blue lines), and others are LH-like (red lines). (b) The envelope functions $\phi_v'^{(U,n',k_t=0)}(z)$ [$v = 1-4$; conduction (red), HH (blue), LH (green), and SO (cyan)] at the BZ center for the first ($n' = 1$) valence subband (HH1). Only the HH component is present. (c) The counterpart of the third ($n' = 3$) valence subband (LH1). The noticeable band mixing exists despite a significant LH part.

functions labeled by $\sigma = L$ are similar to their counterparts labeled by $\sigma = U$ except for proper sign changes of some components, and hence they are not illustrated. From Fig. 2(b), only the HH component is present in the HH1 ($n' = 1$) subband at the BZ center. No couplings to other components occur for this state. The envelop function of the HH1 subband at $k_t = 0$ is symmetric (even parity). On the other hand, the band mixing does occur in the first LH-like state which have opposite parities ($n' = 3$). As shown in Fig. 2(c), while the LH component of LH1 state is dominant, its conduction and SO counterparts are not negligible. The significant band mixing between conduction and valence bands often occurs in the narrow-bandgap semiconductors and type-II nanostructures. That is the reason why the eight-band approach rather than that based on the decoupled six-band and two-band Hamiltonians have to be utilized here.

In calculations of the response field $F_{j,l}^{(n,k_t,s)}(z,\omega')$, the two PMLs which model open regions at two ends of the computation domain are 6 nm in thickness. The parameters of PMLs in Eq. (17) are set as follows: $m = 2$; $h_z = 0.1$ nm; and $\kappa = 5$ pm. For the absorption spectra $\alpha_i(\omega)$ ($i = x,y,z$), the linewidth Υ_{k_t} and parameter η are set to 6.6 meV (corresponding to 0.1 ps) [34] and 10 μeV, respectively. In addition, we focus on the term $I_{n,k_t,ii}(\omega)$ rather than $I_{n,k_t,ii}(-\omega)$ in Eq. (7a) because the former is usually much more significant than the latter. Note that the lineshape broadening related to $I_{n,k_t,ii}(\omega)$ in Eq. (7b) and (7c) can be divided into two parts: the Lorentzian broadening (Υ_{k_t}) due to various incoherent relaxation and dephasing mechanisms; and intrinsic tunneling broadening and interference characterizing $\text{Im}[2V_{n,k_t,ii}(\omega')]$. Figure 3(a) shows the lineshapes of $\text{Im}[2V_{n,k_t,xx}(\omega')]$ corresponding to the HH1 subband at different wave vectors $\mathbf{k}_t = k_t\hat{x}$ along the [100] crystal axis near the BZ center. As k_t increases, resonant energies of the lineshapes blueshift due to the larger energy differences between the metastable states in the conduction band (turn higher in energy) and bound states in the valence subband [become lower in energy, as indicated in Fig. 2(a)]. In addition, each lineshape in Fig. 3(a) is
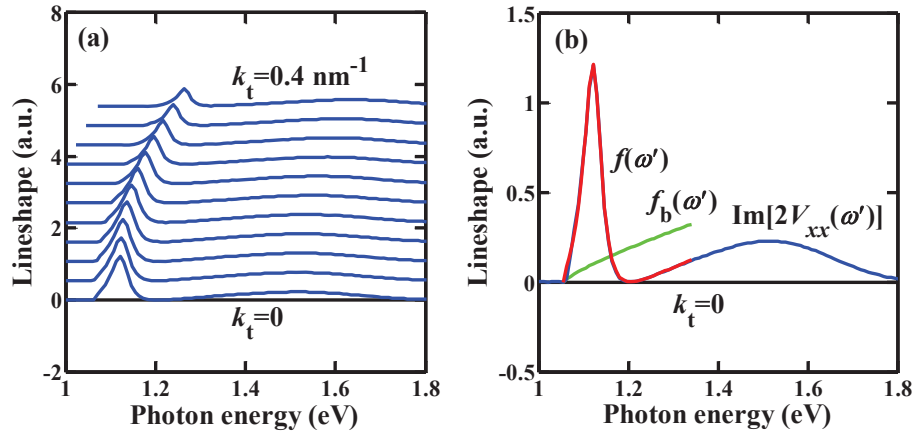
Fig. 3. (a) Lineshapes of $\mathrm{Im}[2V_{n,\mathbf{k}_t,xx}(\omega')]$ corresponding to the HH1 subband at $\mathbf{k}_t = k_t\hat{x}$, where k_t ranges from 0 to 0.4 nm^{-1} at an interval of 0.04 nm^{-1}. All the lineshapes are skew symmetric and exhibit coherent dips at blue sides of their peaks. (b) The fitting function $f(\omega')$ (red) and $\mathrm{Im}[2V_{n,\mathbf{k}_t,xx}(\omega')]$ (blue) of the HH1 subband at the BZ center. The background one $f_b(\omega')$ (green) is also depicted.

skew symmetric and has a dip down to zero at the high-energy side of its peak. These characteristics are commonly present in the Fano resonance due to the coupling between metastable and continuum states [11]. The spectral width of the Fano resonance is a measure of the coupling strength (due to tunneling in this case), and the skewness of the lineshape describes the interferences between the absorptions related to the metastable and continuum states, respectively. If the absorption strengths corresponding to these two types of states are comparable, the skewness of the lineshape becomes prominent. In fact, the zero dip on the lineshape is just a consequence of the coherent interference which happens to be completely destructive at that frequency. Such phenomena, however, are washed out if other incoherent relaxation mechanisms come into play [convolution with the Lorentzian in Eq. (7b)].

To quantify various characteristics of the Fano resonances, we use the following functional form $f(\omega')$ to fit $\mathrm{Im}[2V_{n,\mathbf{k}_t,ii}(\omega')]$ and extract parameters describing couplings between the metastable and continuum states [11]:

$$f(\omega') = f_F(\omega')f_b(\omega'),$$

$$f_F(\omega') = \frac{(\omega' - \omega_r + \gamma_F q/2)^2}{(\omega' - \omega_r)^2 + (\gamma_F/2)^2}, \quad f_b(\omega') = \begin{cases} f_0(\omega'/\omega_b - 1)^{n_b}, & \omega' > \omega_b, \\ 0, & \omega' \le \omega_b, \end{cases} \tag{20}$$

where $f_F(\omega')$ is a function characterizing the Fano resonance; ω_r is the resonant frequency of the transition; γ_F is a linewidth directly related to the coupling strength (tunneling rate); and q is the Fano parameter which measures the relative transition strengths between the metastable and continuum states; $f_b(\omega')$ is a function which phenomenologically models the background transitions due to continuum states; f_0 is a factor describing the magnitude of $f_b(\omega')$; ω_b is an onset energy, beyond which the transitions to continuum states occur; and n_b is an order describing the behavior of $f_b(\omega')$ at $\omega' \gtrsim \omega_b$. As an example, Fig. 3(b) illustrates the function $\mathrm{Im}[2V_{n,\mathbf{k}_t,xx}(\omega')]$ of the HH1 subband at the BZ center, its fitting function $f(\omega')$, and background one $f_b(\omega')$ around the onset frequency ω_b. The agreement between the target lineshape and fitting function are decently satisfactory, which justifies the extractions of various parameters of the Fano resonances through these procedures.
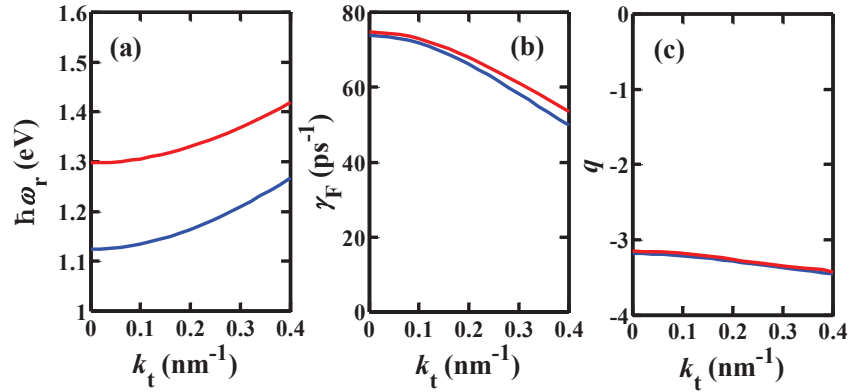
Fig. 4. Parameters of the Fano lineshapes $\mathrm{Im}[2V_{n,\mathbf{k}_t,xx}]$ ($\mathbf{k}_t = k_t\hat{x}$) for the HH1 (blue) and LH1 (red) subbands as a function of k_t: (a) the resonant energy $\hbar\omega_r$; (b) linewidth γ_F; and (c) the Fano parameter q.

With Eq. (20), we extract various parameters related to Fano resonances of the HH1 and LH1 subbands at different wave vectors $\mathbf{k}_t = k_t\hat{x}$ and present them in Fig. 4. From Fig. 4(a), the resonant energies $\hbar\omega_r$ of the HH1 and LH1 subbands both increase with k_t due to the higher energy differences between the initial and final (metastable) states at the larger k_t. The resonant energies of the LH1 subband are larger than those of the HH1 subband due to the lower energies of the LH1 subband, as shown in Fig. 2(a). On the other hand, Fig. 4(b) indicates that the linewidth γ_F becomes smaller as k_t increases. Equivalently, it means that the metastable states at the larger k_t tunnel through the conduction barrier more slowly. This nonintuitive phenomenon may be a result of the more significant effective barrier for conduction states with the larger k_t. From the decoupled two-band model, an electron with a nonvanishing k_t in the conduction band effectively experiences a variation of the barrier potential for tunneling due to the mismatch of the effective masses m_c in neighboring materials. The effective barrier variation $\Delta V_c(k_t)$ can be written as $\Delta V_c(k_t) = (m_{c,\mathrm{GaAsSb}}^{-1} - m_{c,\mathrm{GaAs}}^{-1})\hbar^2 k_t^2/2$, where $m_{c,\mathrm{GaAsSb}}$ and $m_{c,\mathrm{GaAs}}$ are the effective masses of $\mathrm{GaAs_{0.7}Sb_{0.3}}$ and GaAs, respectively, which can be obtained from Table 1. Since the effective mass $m_{c,\mathrm{GaAsSb}}$ is smaller than the other one $m_{c,\mathrm{GaAs}}$, the barrier variation seen by an electron in the GaAs region is positive and increases with k_t. As a result, the corresponding tunneling rate decreases as k_t increases, which qualitatively agrees with the trend in Fig. 4(b). Note that the trend in Fig. 4(b) is merely the outcome of coherent tunneling. In the presence of other tunneling processes assisted by various scattering mechanisms, the overall tunneling rate is not necessarily a decreasing function of k_t. In Fig. 4(c), the magnitudes of the Fano parameters $|q|$ are around 3.1 to 3.5. From these Fano parameters, the ratios between the absorptions due to the metastable and continuum states (within the bandwidths γ_F), which are roughly $\pi q^2/2$ [11], range from 15 to 19 at $k_t \in [0,\ 0.4]$ nm^{-1} for this type-II nanostructure.

The alternative interpretation of linewidths γ_F extracted from Fano lineshapes is just the coherent tunneling rate, and their inverses are the tunneling lifetime of carriers in the metastable states. Figure 5(a) shows the tunneling rate (linewidth) γ_F as a function of the width of $\mathrm{GaAs_{0.7}Sb_{0.3}}$ layers at $k_t = 0$. In the presence of the thinner barrier, the conduction electrons in the metastable states tunnel through the potential barriers more efficiently so that the tunneling rate is higher. Also, the tunneling rate decreases exponentially as the barrier width increases. In Fig. 5(b), we present the polarized absorption spectra $\alpha_i(\omega)$ ($i = x,y,z$) when the $\mathrm{GaAs_{0.7}Sb_{0.3}}$ layer is 2 nm in width. The Lorentzian broadening with $\Upsilon_{\mathbf{k}_t} = 6.6$ meV is included in the calcu-

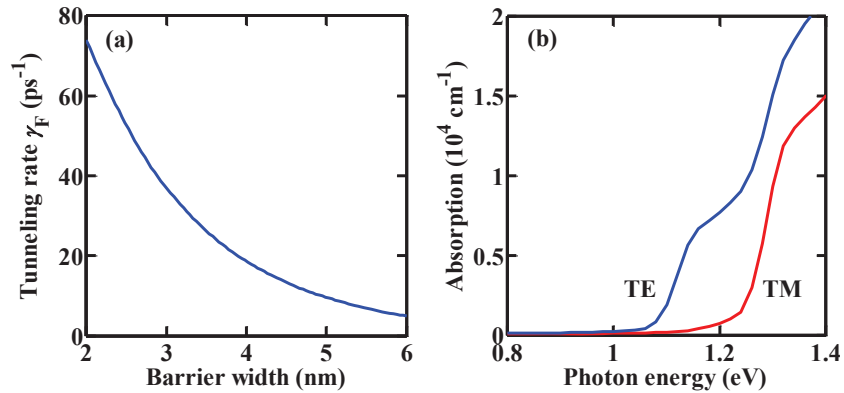Fig. 5. (a) The tunneling rate (linewidth) γ_F versus the width of GaAs$_{0.7}$Sb$_{0.3}$ layers at the BZ center. The rate decreases exponentially as the barrier width increases. (b) The polarized absorption spectra for type-II coupled QWs with a 2 nm GaAs$_{0.7}$Sb$_{0.3}$ layer. The TE absorption (blue) is more significant than TM one (red) at low photon energies.

lation [Eq. (7b)]. The TE absorption is larger than the TM counterpart at low photon energies. The phenomenon is a result of the optical transitions related to the first two HH-like subbands. These transitions provide significant momentum matrix elements parallel to the QW plane at the photon energies around the onset of the absorption. Therefore, the absorption of TE-polarized fields become favored at those photon energies.

4. Conclusion

In summary, we have converted calculations of bound-to-continuum absorption spectra of type-II coupled QWs into an effective source-radiation problem in the eight-band space of the LK and BP Hamiltonians. We utilize PMLs in this multiband space to setup the presence of quasi-bound states. In this way, the tunneling effect inherent in these states is fully taken into account without interferences from the finite size of the computation domain. We further apply these procedures to GaAs$_{0.7}$Sb$_{0.3}$/GaAs type-II coupled QWs and extract various important parameters related to the Fano resonances in this structure. From these Fano lineshapes, the tunneling rates of the metastable states and TE- and TM-polarized absorption spectra can all be obtained unambiguously. In this way, the presented formulation can be helpful in evaluations of carrier extraction efficiencies for type-II nanostructures in photovoltaic applications.

A. Bloch parts and matrix elements of eight-band effective Hamiltonian

The eight Bloch parts adopted in the multiband calculations can be presented in the form of $|j_l, m_l\rangle$ ($l = 1 - 8$), where j_l and m_l are the total angular momentum and magnetic quantum numbers of band l, respectively, which are analogous to those of hydrogen atoms in the presence of spin-orbit coupling. These Bloch parts and their alternative forms are listed in table 2 [18]. Here, Bloch parts $|u_1\rangle$ and $|u_2\rangle$ are assigned as two conduction (C) bands; $|u_3\rangle$ and $|u_6\rangle$ as two HH bands; $|u_4\rangle$ and $|u_5\rangle$ as two LH bands; and $|u_7\rangle$ and $|u_8\rangle$ as two SO bands.

The matrix elements $H_{l'l}[\mathbf{k}]$ of the eight-band effective Hamiltonian for bulk semiconductors (indices l and l' follow the order of Bloch parts in table 2) contain contributions from the LK Hamiltonian [14] and BP strain terms [19]. In the matrix form, this effective Hamiltonian is

Table 2. The eight Bloch parts adopted in the eight-band effective Hamiltonian. Symbols S, X, Y, and Z indicate that the corresponding spatial distributions are similar to the s, x, y, and z orbitals in hydrogen atoms, and $\uparrow$ and $\downarrow$ are the two spin states.

$|u_l\rangle$	$|j_l, m_l\rangle$	Alternative form	Type
$|u_1\rangle$	$|1/2, 1/2\rangle$	$|iS, \uparrow\rangle$	C
$|u_2\rangle$	$|1/2, -1/2\rangle$	$|iS, \downarrow\rangle$	C
$|u_3\rangle$	$|3/2, 3/2\rangle$	$-\left|\frac{X+iY}{\sqrt{2}}, \uparrow\right\rangle$	HH
$|u_4\rangle$	$|3/2, 1/2\rangle$	$-\frac{1}{\sqrt{3}}\left|\frac{X+iY}{\sqrt{2}}, \downarrow\right\rangle + \sqrt{\frac{2}{3}}|Z, \uparrow\rangle$	LH
$|u_5\rangle$	$|3/2, -1/2\rangle$	$\frac{1}{\sqrt{3}}\left|\frac{X-iY}{\sqrt{2}}, \uparrow\right\rangle + \sqrt{\frac{2}{3}}|Z, \downarrow\rangle$	LH
$|u_6\rangle$	$|3/2, -3/2\rangle$	$\left|\frac{X-iY}{\sqrt{2}}, \downarrow\right\rangle$	HH
$|u_7\rangle$	$|1/2, 1/2\rangle$	$\sqrt{\frac{2}{3}}\left|\frac{X+iY}{\sqrt{2}}, \downarrow\right\rangle + \frac{1}{\sqrt{3}}|Z, \uparrow\rangle$	SO
$|u_8\rangle$	$|1/2, -1/2\rangle$	$\sqrt{\frac{2}{3}}\left|\frac{X-iY}{\sqrt{2}}, \uparrow\right\rangle - \frac{1}{\sqrt{3}}|Z, \downarrow\rangle$	SO

expressed as [16]

$$\mathbf{H}[\mathbf{k}] =$$

$$\begin{pmatrix}
E_c+P_c & 0 & -\sqrt{3}V_+ & \sqrt{2}U & V_- & 0 & U & \sqrt{2}V_- \\
0 & E_c+P_c & 0 & -V_+ & \sqrt{2}U & \sqrt{3}V_- & \sqrt{2}V_+ & -U \\
-\sqrt{3}V_- & 0 & E_v-P-Q & S & -R & 0 & \frac{1}{\sqrt{2}}S & -\sqrt{2}R \\
\sqrt{2}U & -V_- & S^* & E_v-P+Q & 0 & -R & \sqrt{2}Q & -\sqrt{\frac{3}{2}}S \\
V_+ & \sqrt{2}U & -R^* & 0 & E_v-P+Q & -S & -\sqrt{\frac{3}{2}}S^* & -\sqrt{2}Q \\
0 & \sqrt{3}V_+ & 0 & -R^* & -S^* & E_v-P-Q & \sqrt{2}R^* & \frac{1}{\sqrt{2}}S^* \\
U & \sqrt{2}V_- & \frac{1}{\sqrt{2}}S^* & \sqrt{2}Q & -\sqrt{\frac{3}{2}}S & \sqrt{2}R & E_v-P-\Delta & 0 \\
\sqrt{2}V_+ & -U & -\sqrt{2}R^* & -\sqrt{\frac{3}{2}}S^* & -\sqrt{2}Q & \frac{1}{\sqrt{2}}S & 0 & E_v-P-\Delta
\end{pmatrix}. \quad (21)$$

On the diagonal of $\mathbf{H}[\mathbf{k}]$ in Eq. (21), energies E_c and E_v are the unstrained conduction and valence bandedges, respectively, and Δ is the spin-orbit split-off energy. Other terms related to the matrix elements within conduction bands or valence bands are [16, 18]

$$P_c = P_{c,\mathbf{k}} + P_{c,\varepsilon}, \quad P = P_\mathbf{k} + P_\varepsilon, \quad Q = Q_\mathbf{k} + Q_\varepsilon, \quad R = R_\mathbf{k} + R_\varepsilon, \quad S = S_\mathbf{k} + S_\varepsilon, \quad (22)$$

where the contributions $P_{c,\mathbf{k}}$, $P_\mathbf{k}$, $Q_\mathbf{k}$, $R_\mathbf{k}$, and $S_\mathbf{k}$ from the LK Hamiltonian are related to the inverse of the bare relative effective mass γ_c in conduction bands, bare Luttinger parameters γ_i ($i = 1, 2, 3$), and various wave-vector components as

$$P_{c,\mathbf{k}} = \left(\frac{\hbar^2}{2m_0}\right)\gamma_c(k_\mathrm{t}^2 + k_z^2), \quad P_\mathbf{k} = \left(\frac{\hbar^2}{2m_0}\right)\gamma_1(k_\mathrm{t}^2 + k_z^2), \quad Q_\mathbf{k} = \left(\frac{\hbar^2}{2m_0}\right)\gamma_2(k_\mathrm{t}^2 - 2k_z^2),$$

$$R_\mathbf{k} = \left(\frac{\hbar^2}{2m_0}\right)\sqrt{3}\left[-\gamma_2(k_x^2 - k_y^2) + i2\gamma_3 k_x k_y\right], \quad S_\mathbf{k} = \left(\frac{\hbar^2}{2m_0}\right)2\sqrt{3}\gamma_3 k_- k_z,$$

$$k_\pm = k_x \pm ik_y = k_\mathrm{t}e^{\pm i\theta}, \quad \theta = \arg[k_+], \quad (23)$$

and the BP strain terms $P_{c,\varepsilon}$, P_ε, Q_ε, R_ε, and S_ε are characterized by deformation potentials a_c,

a_v, b, and d and strain tensors ε_{ij} $(i, j = x, y, z)$:

$$P_{c,\varepsilon} = a_c(\varepsilon_{xx} + \varepsilon_{yy} + \varepsilon_{zz}), \quad P_{\varepsilon} = -a_v(\varepsilon_{xx} + \varepsilon_{yy} + \varepsilon_{zz}), \quad Q_{\varepsilon} = -\frac{b}{2}(\varepsilon_{xx} + \varepsilon_{yy} - 2\varepsilon_{zz}),$$

$$R_{\varepsilon} = \frac{\sqrt{3}b}{2}(\varepsilon_{xx} - \varepsilon_{yy}) - id\varepsilon_{xy}, \quad S_{\varepsilon} = -d(\varepsilon_{xz} - i\varepsilon_{yz}). \tag{24}$$

For QWs grown along the [001] (z) crystal axis on an infinitely thick substrate, the strain tensors due to the lattice mismatch are $\varepsilon_{xx} = \varepsilon_{yy} = (a_0 - a)/a$, $\varepsilon_{zz} = -(2C_{12}/C_{11})\varepsilon_{xx}$, and $\varepsilon_{xy} = \varepsilon_{yz} = \varepsilon_{xz} = 0$, where a_0 and a are the lattice constants of the substrate and QWs, respectively, and C_{11} and C_{12} are the stiffness constants of QWs [18]. In addition to the terms in Eqs. (23) and (24), those associated with the matrix elements between conduction and valence bands are

$$V_{\pm} = \frac{1}{\sqrt{6}}\left(\frac{\hbar}{m_0}\right)P_{cv}k_{\pm}, \quad U = \frac{1}{\sqrt{3}}\left(\frac{\hbar}{m_0}\right)P_{cv}k_z, \quad P_{cv} = \langle iS|p_x|X\rangle = \langle iS|p_y|Y\rangle = \langle iS|p_z|Z\rangle, \tag{25}$$

where P_{cv} is the interband momentum-matrix element.

The inverse of bare relative effective mass γ_c in conduction bands and bare Luttinger parameters γ_i $(i = 1, 2, 3)$ in the eight-band effective Hamiltonian can be extracted from the effective mass m_c in conduction bands and typical Luttinger parameters γ_i^L $(i = 1, 2, 3)$ in the scheme of decoupled conduction and valence-band (six-band) effective Hamiltonians [17]:

$$\gamma_c = \frac{m_0}{m_c} - \frac{E_p(E_g + 2\Delta/3)}{E_g(E_g + \Delta)},$$

$$\gamma_1 = \gamma_1^L - \frac{E_p}{3E_g + \Delta}, \quad \gamma_2 = \gamma_2^L - \frac{1}{2}\left(\frac{E_p}{3E_g + \Delta}\right), \quad \gamma_3 = \gamma_3^L - \frac{1}{2}\left(\frac{E_p}{3E_g + \Delta}\right), \tag{26}$$

where $E_g = E_c - E_v$ is the bandgap energy; and the optical matrix parameter E_p is $2|P_{cv}|^2/m_0$. Equation (26) is utilized to convert m_c and γ_i^L $(i = 1, 2, 3)$ which are commonly available in literature into γ_c and γ_i $(i = 1, 2, 3)$ in the eight-band case.

B. Axial approximation

Under the axial approximation [18], we approximate the term $R_{\mathbf{k}}$ in Eq. (23) as $R_{\mathbf{k}} \simeq -\hbar^2\sqrt{3}(\gamma_2 + \gamma_3)k_-^2/(4m_0)$. Based on this approximation, we carry out the basis transformation that eliminates the in-plane directional dependence on wave vector $\mathbf{k}_t$ [the θ dependence in Eq. (23)] and block-diagonalizes the Hamiltonian matrix $\mathbf{H}[\mathbf{k}]$: $|u'_a\rangle = \sum_l [\mathbf{U}^T(\theta)]_{al}|u_l\rangle$, where $\mathbf{U}^T(\theta)$ means the transpose of the unitary transformation matrix $\mathbf{U}(\theta)$, which is written as

$$\mathbf{U}(\theta) = \frac{1}{\sqrt{2}}\begin{pmatrix} e^{-i\theta/2} & 0 & 0 & 0 & e^{-i\theta/2} & 0 & 0 & 0 \\ ie^{i\theta/2} & 0 & 0 & 0 & -ie^{i\theta/2} & 0 & 0 & 0 \\ 0 & e^{-i3\theta/2} & 0 & 0 & 0 & e^{-i3\theta/2} & 0 & 0 \\ 0 & 0 & ie^{-i\theta/2} & 0 & 0 & 0 & -ie^{-i\theta/2} & 0 \\ 0 & 0 & -e^{i\theta/2} & 0 & 0 & 0 & -e^{i\theta/2} & 0 \\ 0 & -ie^{i3\theta/2} & 0 & 0 & 0 & ie^{i3\theta/2} & 0 & 0 \\ 0 & 0 & 0 & -ie^{-i\theta/2} & 0 & 0 & 0 & ie^{-i\theta/2} \\ 0 & 0 & 0 & -e^{i\theta/2} & 0 & 0 & 0 & -e^{i\theta/2} \end{pmatrix}. \tag{27}$$

If the BP strain terms R_{ε} and S_{ε} vanish, the matrix $\mathbf{U}(\theta)$ transforms the effective Hamiltonian $\mathbf{H}[\mathbf{k}]$ of bulk semiconductors in Eq. (21) into a block-diagonal Hamiltonian $\mathbf{H}'[k_t, k_z]$ that is independent of angle θ: [15, 16]

$$\mathbf{H}'[k_t, k_z] = \mathbf{U}(\theta)^{\dagger}\mathbf{H}[\mathbf{k}]\mathbf{U}(\theta) = \begin{pmatrix} \mathbf{H}^U[k_t, k_z] & \mathbf{0}_{4\times 4} \\ \mathbf{0}_{4\times 4} & \mathbf{H}^L[k_t, k_z] \end{pmatrix}, \tag{28}$$

where $\mathbf{0}_{4\times4}$ is the 4-by-4 null matrix; and the upper and lower 4-by-4 Hamiltonian matrices $\mathbf{H}^{\mathrm{U}}[k_{\mathrm{t}}, k_z]$ and $\mathbf{H}^{\mathrm{L}}[k_{\mathrm{t}}, k_z]$ are

$$
\mathbf{H}^{\mathrm{U}}[k_{\mathrm{t}}, k_z] = \begin{pmatrix} E_c + P_c & -\sqrt{3}V_\rho & -V_\rho + i\sqrt{2}U & -\sqrt{2}V_\rho - iU \\ -\sqrt{3}V_\rho & E_v - P - Q & R_\rho + iS_\rho & \sqrt{2}R_\rho - i\frac{1}{\sqrt{2}}S_\rho \\ -V_\rho - i\sqrt{2}U & R_\rho - iS_\rho & E_v - P + Q & -\sqrt{2}Q - i\sqrt{\frac{3}{2}}S_\rho \\ -\sqrt{2}V_\rho + iU & \sqrt{2}R_\rho + i\frac{1}{\sqrt{2}}S_\rho & -\sqrt{2}Q + i\sqrt{\frac{3}{2}}S_\rho & E_v - P - \Delta \end{pmatrix}, \quad (29)
$$

and $\mathbf{H}^{\mathrm{L}}[k_{\mathrm{t}}, k_z] = \mathbf{H}^{\mathrm{U}*}[k_{\mathrm{t}}, k_z]$, where the terms V_ρ, R_ρ, and S_ρ are θ-independent and are given as

$$
V_\rho = \frac{1}{\sqrt{6}}\left(\frac{\hbar}{m_0}\right)P_{cv}k_{\mathrm{t}}, \;\; R_\rho = -\left(\frac{\hbar^2}{2m_0}\right)\sqrt{3}\left(\frac{\gamma_2 + \gamma_3}{2}\right)k_{\mathrm{t}}^2, \;\; S_\rho = \left(\frac{\hbar^2}{2m_0}\right)2\sqrt{3}\gamma_3 k_{\mathrm{t}}k_z. \quad (30)
$$

We denote the 8-by-1 column vector composed of envelop functions $\phi_l^{(n,\mathbf{k})}$ in band n of the bulk Hamiltonian matrix $\mathbf{H}[\mathbf{k}]$ as $\mathbf{\Phi}^{(n,\mathbf{k})}$, namely, $[\mathbf{\Phi}^{(n,\mathbf{k})}]_{l,1} = \phi_l^{(n,\mathbf{k})}$ [the factor $\exp(i\mathbf{k}\cdot\mathbf{r})$ is not included in envelop functions here]. The vector $\mathbf{\Phi}^{(n,\mathbf{k})}$ is an eigenvector of $\mathbf{H}[\mathbf{k}]$ in Eq. (21). The eigenvectors $\mathbf{\Phi}'^{(n,k_{\mathrm{t}},k_z)}$ corresponding to $\mathbf{H}'[k_{\mathrm{t}}, k_z]$ can be classified based on whether they are merely composed of the 4-by-1 eigenvectors of $\mathbf{H}^{\mathrm{U}}[k_{\mathrm{t}}, k_z]$ or those of $\mathbf{H}^{\mathrm{L}}[k_{\mathrm{t}}, k_z]$:

$$
\mathbf{\Phi}'^{(n,k_{\mathrm{t}},k_z)} = \begin{pmatrix} \mathbf{\Phi}'^{(\mathrm{U},n',k_{\mathrm{t}},k_z)} \\ \mathbf{0}_{4\times1} \end{pmatrix} \text{ or } \begin{pmatrix} \mathbf{0}_{4\times1} \\ \mathbf{\Phi}'^{(\mathrm{L},n',k_{\mathrm{t}},k_z)} \end{pmatrix}, \quad (31)
$$

where $\mathbf{0}_{4\times1}$ is the 4-by-1 null vector; the band label $n = (\sigma, n')$ now includes an index σ indicating the upper (U) or lower (L) eigenvectors and another one n' referring to other types of splittings; and $\mathbf{\Phi}'^{(\mathrm{U},n',k_{\mathrm{t}},k_z)}$ and $\mathbf{\Phi}'^{(\mathrm{L},n',k_{\mathrm{t}},k_z)}$ are eigenvectors of $\mathbf{H}^{\mathrm{U}}[k_{\mathrm{t}}, k_z]$ and $\mathbf{H}^{\mathrm{L}}[k_{\mathrm{t}}, k_z]$, respectively. Inspections of Bloch parts $|u'_v\rangle$ indicate that the first to the last envelop functions of $\mathbf{\Phi}'^{(\sigma,n',k_{\mathrm{t}},k_z)}$ belong to the conduction, HH, LH, and SO bands, respectively. Once the eigenvectors $\mathbf{\Phi}'^{(n,k_{\mathrm{t}},k_z)}$ and their energies $E_{n,k_{\mathrm{t}},k_z} \equiv E_{n',k_{\mathrm{t}},k_z}^\sigma$ are solved, we then transform these vectors back to $\mathbf{\Phi}^{(n,\mathbf{k})}$: $\mathbf{\Phi}^{(n,\mathbf{k})} = \mathbf{U}(\theta)\mathbf{\Phi}'^{(n,k_{\mathrm{t}},k_z)}$, where the θ dependence of $\mathbf{\Phi}^{(n,\mathbf{k})}$ merely originates from matrix $\mathbf{U}(\theta)$ under the axial approximation.

As to the axial approximation for QW nanostructures in which the BP terms $R_\varepsilon(z)$ and $S_\varepsilon(z)$ vanish, the above procedures still apply even if the hermitian forms in Eq. (3) are used. The only difference is that the k_z dependencies of various envelop functions and eigenenergies $E_{n,k_{\mathrm{t}}} \equiv E_{n',k_{\mathrm{t}}}^\sigma$ are converted to the real-space dependence of z and incorporated into label n', respectively. Once the eigenenergy problem corresponding to envelop functions $\phi_v'^{(\sigma,n',k_{\mathrm{t}})}(z)$ $(v = 1 - 4)$ of the eigenvector $\mathbf{\Phi}'^{(\sigma,n',k_{\mathrm{t}})}(z)$ is solved:

$$
\sum_{v=1}^{4} H_{v'v}^\sigma[k_{\mathrm{t}}, k_z = -i\partial_z]\phi_v'^{(\sigma,n',k_{\mathrm{t}})}(z) = E_{n',k_{\mathrm{t}}}^\sigma \phi_{v'}'^{(\sigma,n',k_{\mathrm{t}})}(z), \quad (32)
$$

we then transform the vectors $\mathbf{\Phi}'^{(n,k_{\mathrm{t}})}(z)$ which are composed of $\mathbf{\Phi}'^{(\sigma,n',k_{\mathrm{t}})}(z)$ back to $\mathbf{\Phi}^{(n,\mathbf{k}_{\mathrm{t}})}(z)$: $\mathbf{\Phi}^{(n,\mathbf{k}_{\mathrm{t}})}(z) = \mathbf{U}(\theta)\mathbf{\Phi}'^{(n,k_{\mathrm{t}})}(z)$. In this way, the envelop functions $\phi_l^{(n,\mathbf{k}_{\mathrm{t}})}(z)$ that constitute $\mathbf{\Phi}^{(n,\mathbf{k}_{\mathrm{t}})}(z)$ are obtained.

C. Matrices $\mathbf{\Gamma}$, $\mathbf{Q}$, and $\mathbf{\Lambda}[\mathbf{k}_{\mathrm{t}}]$

For simplicity, rather than representing the 8-by-8 matrices $\mathbf{\Gamma}$, $\mathbf{Q}$, and $\mathbf{\Lambda}[\mathbf{k}_{\mathrm{t}}]$ with their cartesian components, of which the corresponding matrix elements are complex, we rearrange them

partially in terms of the circularly-polarized $[\hat{e}_\pm = (\hat{x} \pm i\hat{y})/\sqrt{2}]$ and z components as

$$\boldsymbol{\Gamma} = \boldsymbol{\Gamma}_+ \hat{e}_+ + \boldsymbol{\Gamma}_- \hat{e}_- + \boldsymbol{\Gamma}_z \hat{z},$$
$$\mathbf{Q} = \mathbf{Q}_+ \hat{e}_+ + \mathbf{Q}_- \hat{e}_- + \mathbf{Q}_z \hat{z},$$
$$\boldsymbol{\Lambda}(\mathbf{k}_t) = \boldsymbol{\Lambda}_t \mathbf{k}_t + [\boldsymbol{\Lambda}_1 + \boldsymbol{\Lambda}_2]k_+ \hat{e}_+ + [\boldsymbol{\Lambda}_{-1} + \boldsymbol{\Lambda}_{-2}]k_- \hat{e}_- + [\boldsymbol{\Lambda}_{z,+}k_+ + \boldsymbol{\Lambda}_{z,-}k_-]\hat{z}. \tag{33}$$

The expressions of some matrices in Eq. (33) are [25, 26]

$$\boldsymbol{\Gamma}_+ = \frac{P_{cv}}{\sqrt{3}} \begin{pmatrix} 0 & 0 & -\sqrt{3} & 0 & 0 & 0 & 0 & 0 \\ 0 & 0 & 0 & -1 & 0 & 0 & \sqrt{2} & 0 \\ 0 & 0 & 0 & 0 & 0 & 0 & 0 & 0 \\ 0 & 0 & 0 & 0 & 0 & 0 & 0 & 0 \\ 1 & 0 & 0 & 0 & 0 & 0 & 0 & 0 \\ 0 & \sqrt{3} & 0 & 0 & 0 & 0 & 0 & 0 \\ 0 & 0 & 0 & 0 & 0 & 0 & 0 & 0 \\ \sqrt{2} & 0 & 0 & 0 & 0 & 0 & 0 & 0 \end{pmatrix}, \quad \boldsymbol{\Gamma}_z = \frac{P_{cv}}{\sqrt{3}} \begin{pmatrix} 0 & 0 & 0 & \sqrt{2} & 0 & 0 & 1 & 0 \\ 0 & 0 & 0 & 0 & \sqrt{2} & 0 & 0 & -1 \\ 0 & 0 & 0 & 0 & 0 & 0 & 0 & 0 \\ \sqrt{2} & 0 & 0 & 0 & 0 & 0 & 0 & 0 \\ 0 & \sqrt{2} & 0 & 0 & 0 & 0 & 0 & 0 \\ 0 & 0 & 0 & 0 & 0 & 0 & 0 & 0 \\ 1 & 0 & 0 & 0 & 0 & 0 & 0 & 0 \\ 0 & -1 & 0 & 0 & 0 & 0 & 0 & 0 \end{pmatrix},$$

$$\mathbf{Q}_+ = \gamma_3 \begin{pmatrix} 0 & 0 & 0 & 0 & 0 & 0 & 0 & 0 \\ 0 & 0 & 0 & 0 & 0 & 0 & 0 & 0 \\ 0 & 0 & 0 & 0 & 0 & 0 & 0 & 0 \\ 0 & 0 & \sqrt{6} & 0 & 0 & 0 & 0 & 0 \\ 0 & 0 & 0 & 0 & 0 & 0 & -3 & 0 \\ 0 & 0 & 0 & 0 & -\sqrt{6} & 0 & 0 & \sqrt{3} \\ 0 & 0 & \sqrt{3} & 0 & 0 & 0 & 0 & 0 \\ 0 & 0 & 0 & -3 & 0 & 0 & 0 & 0 \end{pmatrix}, \quad \boldsymbol{\Lambda}_1 = \frac{\gamma_2 + \gamma_3}{\sqrt{2}} \begin{pmatrix} 0 & 0 & 0 & 0 & 0 & 0 & 0 & 0 \\ 0 & 0 & 0 & 0 & 0 & 0 & 0 & 0 \\ 0 & 0 & 0 & 0 & 0 & 0 & 0 & 0 \\ 0 & 0 & 0 & 0 & 0 & 0 & 0 & 0 \\ 0 & 0 & \sqrt{3} & 0 & 0 & 0 & 0 & 0 \\ 0 & 0 & 0 & \sqrt{3} & 0 & 0 & -\sqrt{6} & 0 \\ 0 & 0 & 0 & 0 & 0 & 0 & 0 & 0 \\ 0 & 0 & \sqrt{6} & 0 & 0 & 0 & 0 & 0 \end{pmatrix},$$

$$\boldsymbol{\Lambda}_t = \begin{pmatrix} \gamma_c & 0 & 0 & 0 & 0 & 0 & 0 & 0 \\ 0 & \gamma_c & 0 & 0 & 0 & 0 & 0 & 0 \\ 0 & 0 & -\gamma_1 - \gamma_2 & 0 & 0 & 0 & 0 & 0 \\ 0 & 0 & 0 & -\gamma_1 + \gamma_2 & 0 & 0 & \sqrt{2}\gamma_2 & 0 \\ 0 & 0 & 0 & 0 & -\gamma_1 + \gamma_2 & 0 & 0 & -\sqrt{2}\gamma_2 \\ 0 & 0 & 0 & 0 & 0 & -\gamma_1 - \gamma_2 & 0 & 0 \\ 0 & 0 & 0 & \sqrt{2}\gamma_2 & 0 & 0 & -\gamma_1 & 0 \\ 0 & 0 & 0 & 0 & -\sqrt{2}\gamma_2 & 0 & 0 & -\gamma_1 \end{pmatrix},$$

and $\mathbf{Q}_z = \boldsymbol{\Lambda}_t[\gamma_2 \to -2\gamma_2]$, $\boldsymbol{\Lambda}_2 = \boldsymbol{\Lambda}_1^{\mathrm{T}}(\gamma_2 - \gamma_3)/(\gamma_2 + \gamma_3)$, $\boldsymbol{\Lambda}_{z,+} = \mathbf{Q}_+/\sqrt{2}$. In addition, we have $\boldsymbol{\Gamma}_- = \boldsymbol{\Gamma}_+^{\mathrm{T}}$; $\mathbf{Q}_- = \mathbf{Q}_+^{\mathrm{T}}$; $\boldsymbol{\Lambda}_{-1} = \boldsymbol{\Lambda}_1^{\mathrm{T}}$; $\boldsymbol{\Lambda}_{-2} = \boldsymbol{\Lambda}_2^{\mathrm{T}}$; and $\boldsymbol{\Lambda}_{z,-} = \boldsymbol{\Lambda}_{z,+}^{\mathrm{T}}$. Note that the factor $\gamma_2 - \gamma_3$ is dropped in the axial approximation, and therefore matrices $\boldsymbol{\Lambda}_{\pm 2}$ are not required in that case.

Acknowledgments